Available online at www.sciencedirect.com
ScienceDirect
Journal of Computational Physics 227 (2008) 4398–4424
JOURNAL OF COMPUTATIONAL PHYSICS
www.elsevier.com/locate/jcp

Absorbing boundary conditions for nonlinear Euler and Navier–Stokes equations based on the perfectly matched layer technique

Fang Q. Hu [a,*], X.D. Li [b], D.K. Lin [b]

[a] Department of Mathematics and Statistics, Old Dominion University, Norfolk, VA 23529, United States
[b] School of Jet Propulsion, Beihang University, Beijing 100083, People's Republic of China

Received 6 April 2007; received in revised form 5 October 2007; accepted 4 January 2008
Available online 26 January 2008

Abstract

Absorbing boundary conditions for the nonlinear Euler and Navier–Stokes equations in three space dimensions are presented based on the perfectly matched layer (PML) technique. The derivation of equations follows a three-step method recently developed for the PML of linearized Euler equations. To increase the efficiency of the PML, a pseudo mean flow is introduced in the formulation of absorption equations. The proposed PML equations will absorb exponentially the difference between the nonlinear fluctuation and the prescribed pseudo mean flow. With the nonlinearity in flux vectors, the proposed nonlinear absorbing equations are not formally perfectly matched to the governing equations as their linear counter-parts are. However, numerical examples show satisfactory results. Furthermore, the nonlinear PML reduces automatically to the linear PML upon linearization about the pseudo mean flow. The validity and efficiency of proposed equations as absorbing boundary conditions for nonlinear Euler and Navier–Stokes equations are demonstrated by numerical examples.

Keywords: Non-reflecting boundary condition; Perfectly matched layer; Navier–Stokes equations; Euler equations; Computational fluid dynamics; Computational aeroacoustics

1. Introduction

Non-reflecting boundary condition is a critical component in the development of computational fluid dynamics (CFD) and computational aeroacoustics (CAA) algorithms. It remains a significant challenge particularly for problems involving nonlinear governing equations. Perfectly matched layer (PML) is a technique of developing non-reflecting boundary conditions by constructing matched equations that can absorb outgoing waves at open computational boundaries. It was originally designed for computational electro-magnetics [5,6,8,28,27,7]. The significance of the PML technique lies in the fact that the absorbing zone is theoretically

* Corresponding author. Tel.: +1 804 683 3882; fax: +1 804 683 3885.
E-mail address: fang@math.odu.edu (F.Q. Hu).

0021-9991/$ - see front matter © 2008 Elsevier Inc. All rights reserved.
doi:10.1016/j.jcp.2008.01.010

reflectionless for multi-dimensional linear waves of any angle and frequency. In the past few years, substantial progress has been made in the development of the PML technique for the Euler equations, starting with the studies for cases with constant mean flows, followed by extensions to cases with non-uniform mean flows [16,17,14,1,18,19,4,10,9]. Most recently, applications of PML to linearized Navier–Stokes equations and nonlinear Navier–Stokes equations have been discussed in [12,13]. A recent progress review is given in [21].

Although the PML technique itself is relatively simple when it is viewed as a complex change of variables in the frequency domain, it is important to note that, for the PML technique to yield stable absorbing boundary conditions, the phase and group velocities of the physical waves supported by the governing equations must be consistent and in the same direction [3,4,9,18]. For governing equations that support physical waves of inconsistent phase and group velocities, such as the Euler or Navier–Stokes equations for fluid dynamics, a space–time transformation may be required before applying the PML technique in the derivation process [18,19]. This space–time transformation corrects the inconsistency in the phase and group velocities and thus permits the application of the PML technique. An emerging method of formulating PML involves essentially three steps [21]:

1. A proper space–time transformation is determined and applied to the governing equations.
2. A PML complex change of variables is applied in the frequency domain.
3. The time domain absorbing boundary condition is derived by a conversion of the frequency domain equations.

This procedure has been successfully applied to the derivation of PML for the linearized Euler equations in [18,19].

In this paper, further application of the PML technique to the nonlinear Euler and Navier–Stokes equations is considered. Derivation of the absorbing equation is proceeded by applying the three steps outlined above to the nonlinear Navier–Stokes equations, which include the Euler equations as a special case. However, unlike the PML for linear equations, the conversion to time domain equations does not result in formally perfectly matched equations due to the nonlinearity in flux vectors. Nonetheless, the proposed absorbing equations are still effective for nonlinear problem as we will show in numerical examples. Furthermore, the nonlinear PML reduces automatically to the linear PML upon linearization. The current formulation offers a natural extension of the linear PML to nonlinear equations. For convenience of implementation in most existing CFD and CAA codes, all PML equations are formulated for the governing equations in the conservation form.

To absorb the nonlinear disturbances, a concept of "pseudo mean flow" is introduced. This makes the PML possible without knowing the exact mean flow at the start of the computation. Equations are derived that absorb the difference between the pseudo mean flow and the nonlinear disturbances, including the vorticity, acoustic, and entropy waves. One limitation of the current paper is that the pseudo mean flow is assumed to be aligned with one of three spatial axes. Recent efforts and new developments on extending the PML for oblique mean flows can be found in [11,2,24].

The rest of the paper is organized as follows. In the next section, the PML absorbing boundary condition is derived for the nonlinear Navier–Stokes equations. Further discussions on the formulation are given in Section 3. In Section 4, numerical examples that validate the effectiveness and stability of the PML for nonlinear Euler and Navier–Stokes equations will be presented. They include the absorption of a convective isentropic vortex in compressible flows, shear flow vortices and vortices shedded from flow over a circular cylinder, calculation of flat plate boundary layers, and propagation of a 3D acoustic pulse. Concluding remarks are given in Section 5.

2. Derivation of PML equations for nonlinear Navier–Stokes equations

2.1. Governing equations

We consider the three-dimensional compressible nonlinear Navier–Stokes equation written in the conservation form as

$$\frac{\partial \mathbf{u}}{\partial t}+\frac{\partial \mathbf{F}_1}{\partial x}+\frac{\partial \mathbf{F}_2}{\partial y}+\frac{\partial \mathbf{F}_3}{\partial z}=0 \tag{1}$$

where

$$\mathbf{u}=\begin{bmatrix}\rho\\ \rho u\\ \rho v\\ \rho w\\ \rho e\end{bmatrix} \tag{2}$$

and flux vectors

$$\mathbf{F}_1=\begin{bmatrix}\rho u\\ \rho u^2+p-\tau_{xx}\\ \rho uv-\tau_{xy}\\ \rho uw-\tau_{xz}\\ (\rho e+p)u-u\tau_{xx}-v\tau_{xy}-w\tau_{xz}+q_x\end{bmatrix} \tag{3}$$

$$\mathbf{F}_2=\begin{bmatrix}\rho v\\ \rho uv-\tau_{xy}\\ \rho v^2+p-\tau_{yy}\\ \rho vw-\tau_{yz}\\ (\rho e+p)v-u\tau_{xy}-v\tau_{yy}-w\tau_{yz}+q_y\end{bmatrix} \tag{4}$$

$$\mathbf{F}_3=\begin{bmatrix}\rho w\\ \rho uw-\tau_{xz}\\ \rho vw-\tau_{yz}\\ \rho w^2+p-\tau_{zz}\\ (\rho e+p)w-u\tau_{xz}-v\tau_{yz}-w\tau_{zz}+q_z\end{bmatrix} \tag{5}$$

with viscous stress terms written as

$$\tau_{xx}=\frac{M}{Re}\left[2\mu\frac{\partial u}{\partial x}-\lambda\left(\frac{\partial u}{\partial x}+\frac{\partial v}{\partial y}+\frac{\partial w}{\partial z}\right)\right],\quad \tau_{yy}=\frac{M}{Re}\left[2\mu\frac{\partial v}{\partial y}-\lambda\left(\frac{\partial u}{\partial x}+\frac{\partial v}{\partial y}+\frac{\partial w}{\partial z}\right)\right], \tag{6}$$

$$\tau_{zz}=\frac{M}{Re}\left[2\mu\frac{\partial w}{\partial z}-\lambda\left(\frac{\partial u}{\partial x}+\frac{\partial v}{\partial y}+\frac{\partial w}{\partial z}\right)\right],\quad \lambda=\frac{2}{3}\mu \tag{7}$$

$$\tau_{xy}=\frac{M}{Re}\mu\left(\frac{\partial u}{\partial y}+\frac{\partial v}{\partial x}\right),\quad \tau_{xz}=\frac{M}{Re}\mu\left(\frac{\partial u}{\partial z}+\frac{\partial w}{\partial x}\right),\quad \tau_{yz}=\frac{M}{Re}\mu\left(\frac{\partial v}{\partial z}+\frac{\partial w}{\partial y}\right) \tag{8}$$

and heat transfer terms

$$q_x=-\frac{M}{(\gamma-1)PrRe}\mu\frac{\partial T}{\partial x},\quad q_y=-\frac{M}{(\gamma-1)PrRe}\mu\frac{\partial T}{\partial y},\quad q_z=-\frac{M}{(\gamma-1)PrRe}\mu\frac{\partial T}{\partial z} \tag{9}$$

where μ is nondimensionalized viscosity which, unless noted otherwise, will be assumed to be a function of temperature T by the Sutherland's formula [25]. The equation of state and the energy function are

$$\gamma p=\rho T,\quad e=\frac{u^2+v^2+w^2}{2}+\frac{p}{(\gamma-1)\rho} \tag{10}$$

In the above, u, v and w are the velocity components in x, y and z directions, respectively, p is the pressure, ρ is the density, and T is the temperature. The velocity is nondimensionalized by a reference speed of sound a_∞, density by ρ_∞ and pressure by $\rho_\infty a_\infty^2$. Viscosity μ is nondimensionalized by a reference value μ_∞ and

$Re = \rho_\infty U_\infty L_\infty/\mu_\infty$ is the Reynolds number based on a characteristic flow velocity U_∞ and length scale L_∞. M is the Mach number U_∞/a_∞. Pr is the Prandtl number and γ is the specific heats ratio.

To facilitate the derivation of PML equations for (1), we denote $\mathbf{G}(\mathbf{u})$ as a vector that contains all variables whose spatial derivative is present in formulating the flux vectors, i.e.,

$$\mathbf{G}(\mathbf{u}) = \begin{bmatrix} u \\ v \\ w \\ T \end{bmatrix} \tag{11}$$

and introduce new variables $\mathbf{e}_1$, $\mathbf{e}_2$ and $\mathbf{e}_3$ as

$$\mathbf{e}_1 = \frac{\partial \mathbf{G}(\mathbf{u})}{\partial x} \equiv \begin{bmatrix} \frac{\partial u}{\partial x} \\ \frac{\partial v}{\partial x} \\ \frac{\partial w}{\partial x} \\ \frac{\partial T}{\partial x} \end{bmatrix}, \quad \mathbf{e}_2 = \frac{\partial \mathbf{G}(\mathbf{u})}{\partial y} \equiv \begin{bmatrix} \frac{\partial u}{\partial y} \\ \frac{\partial v}{\partial y} \\ \frac{\partial w}{\partial y} \\ \frac{\partial T}{\partial y} \end{bmatrix}, \quad \mathbf{e}_3 = \frac{\partial \mathbf{G}(\mathbf{u})}{\partial z} \equiv \begin{bmatrix} \frac{\partial u}{\partial z} \\ \frac{\partial v}{\partial z} \\ \frac{\partial w}{\partial z} \\ \frac{\partial T}{\partial z} \end{bmatrix} \tag{12}$$

We then re-define the flux vectors of (3)–(5) as explicit functions of $\mathbf{u}$, $\mathbf{e}_1$, $\mathbf{e}_2$ and $\mathbf{e}_3$ and re-write (1) as

$$\frac{\partial \mathbf{u}}{\partial t} + \frac{\partial \mathbf{F}_1(\mathbf{u}, \mathbf{e}_1, \mathbf{e}_2, \mathbf{e}_3)}{\partial x} + \frac{\partial \mathbf{F}_2(\mathbf{u}, \mathbf{e}_1, \mathbf{e}_2, \mathbf{e}_3)}{\partial y} + \frac{\partial \mathbf{F}_3(\mathbf{u}, \mathbf{e}_1, \mathbf{e}_2, \mathbf{e}_3)}{\partial z} = 0 \tag{13}$$

Eqs. (12) and (13) form a system of partial differential equations for unknowns $\mathbf{u}$, $\mathbf{e}_1$, $\mathbf{e}_2$ and $\mathbf{e}_3$. This system is only a re-writing of the original Navier–Stokes equation (1) and thus is equivalent to (1). We note that now the flux vectors $\mathbf{F}_1(\mathbf{u}, \mathbf{e}_1, \mathbf{e}_2, \mathbf{e}_3)$, $\mathbf{F}_2(\mathbf{u}, \mathbf{e}_1, \mathbf{e}_2, \mathbf{e}_3)$ and $\mathbf{F}_3(\mathbf{u}, \mathbf{e}_1, \mathbf{e}_2, \mathbf{e}_3)$ do not explicitly involve spatial derivatives of $\mathbf{u}$. In what follows, we shall derive the PML equations for (12) and (13).

2.2. Pseudo mean flow

As shown in Fig. 1, at non-reflecting boundaries, we introduce PML domains to absorb out-going disturbances. We wish to formulate the equations to be used in the added zones so that out-going waves can be exponentially reduced once they enter the added zones while causing as little numerical reflection as possible. By reducing the disturbances to a negligible level toward the end of the PML domain, the use of PML makes a non-reflecting boundary condition at the outer boundaries of the whole computational domain unnecessary.

In nonlinear simulations, a solution $\mathbf{u}$ of (1) can be regarded as consisting of a time-independent mean state and a time-dependent fluctuation that has to be governed by the nonlinear equations. However, it may not be most efficient to absorb the total variable $\mathbf{u}$ and to reduce it to nearly zero inside the PML domain. On the other hand, the exact mean state is usually not known at the start of the computation. The PML formulation

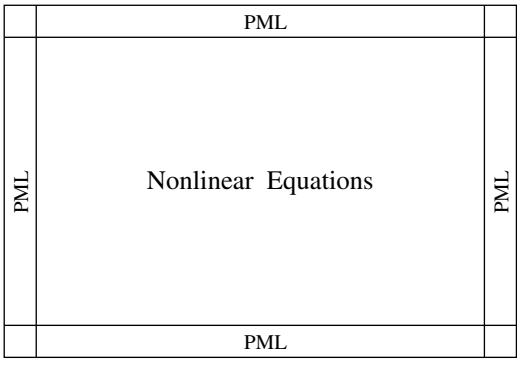

Fig. 1. Schematics of physical and PML domains.

presented here will not require the exact mean flow. Instead, as in [17], we shall partition the solution inside the PML domain into two parts as follows,

$$\mathbf{u} = \bar{\mathbf{u}}_p + \mathbf{u}', \quad \mathbf{e}_1 = \bar{\mathbf{e}}_1 + \mathbf{e}_1', \quad \mathbf{e}_2 = \bar{\mathbf{e}}_2 + \mathbf{e}_2', \quad \mathbf{e}_3 = \bar{\mathbf{e}}_3 + \mathbf{e}_3' \tag{14}$$

with

$$\bar{\mathbf{e}}_1 = \frac{\partial \mathbf{G}(\bar{\mathbf{u}}_p)}{\partial x}, \quad \bar{\mathbf{e}}_2 = \frac{\partial \mathbf{G}(\bar{\mathbf{u}}_p)}{\partial y}, \quad \bar{\mathbf{e}}_3 = \frac{\partial \mathbf{G}(\bar{\mathbf{u}}_p)}{\partial z} \tag{15}$$

where $\bar{\mathbf{u}}_p$ denotes a prescribed time-independent "pseudo mean flow" [17,20]. We only require that the chosen $\bar{\mathbf{u}}_p$ satisfy the steady state equation:

$$\frac{\partial \mathbf{F}_1(\bar{\mathbf{u}}_p, \bar{\mathbf{e}}_1, \bar{\mathbf{e}}_2, \bar{\mathbf{e}}_3)}{\partial x} + \frac{\partial \mathbf{F}_2(\bar{\mathbf{u}}_p, \bar{\mathbf{e}}_1, \bar{\mathbf{e}}_2, \bar{\mathbf{e}}_3)}{\partial y} + \frac{\partial \mathbf{F}_3(\bar{\mathbf{u}}_p, \bar{\mathbf{e}}_1, \bar{\mathbf{e}}_2, \bar{\mathbf{e}}_3)}{\partial z} = 0 \tag{16}$$

It is important to emphasize that this pseudo mean flow is not required to be the exact mean flow at the non-reflecting boundary. The use of $\bar{\mathbf{u}}_p$ is to make the PML domain more efficient since we now need only to absorb $\mathbf{u}'$, $\mathbf{e}_1'$, $\mathbf{e}_2'$ and $\mathbf{e}_3'$, namely, the differences between total flow variables and that of a prescribed pseudo mean flow, as illustrated in Fig. 2. In practical computations, any known steady state solution that resembles the actual flow could serve as a pseudo mean flow. It also follows that the choice for $\bar{\mathbf{u}}_p$ is not unique. Of course, the closer the pseudo mean flow is to the actual mean flow the better.

By (12)–(16), the governing equations for $\mathbf{u}'$, $\mathbf{e}_1'$, $\mathbf{e}_2'$ and $\mathbf{e}_3'$ are

$$\frac{\partial \mathbf{u}'}{\partial t} + \frac{\partial [\mathbf{F}_1 - \overline{\mathbf{F}}_1]}{\partial x} + \frac{\partial [\mathbf{F}_2 - \overline{\mathbf{F}}_2]}{\partial y} + \frac{\partial [\mathbf{F}_3 - \bar{\mathbf{F}}_3]}{\partial z} = 0 \tag{17}$$

$$\mathbf{e}_1' = \frac{\partial [\mathbf{G} - \overline{\mathbf{G}}]}{\partial x}, \quad \mathbf{e}_2' = \frac{\partial [\mathbf{G} - \overline{\mathbf{G}}]}{\partial y}, \quad \mathbf{e}_3' = \frac{\partial [\mathbf{G} - \overline{\mathbf{G}}]}{\partial z} \tag{18}$$

For brevity, the arguments for the flux vectors $\mathbf{F}_1$, $\mathbf{F}_2$, $\mathbf{F}_3$ and vector $\mathbf{G}$ are not shown explicitly in (17) and (18), and an over-bar indicates that the vector is computed using the pseudo mean flow. We shall now derive the PML equations that absorb $\mathbf{u}'$, $\mathbf{e}_1'$, $\mathbf{e}_2'$ and $\mathbf{e}_3'$.

2.3. Formulation of PML equations

We will assume in the present paper that the pseudo mean flow is in the direction of x-axis. By following the three-step method for the derivation of PML described in Introduction, we first apply a space–time transformation of the form

$$\bar{t} = t + \beta x \tag{19}$$

to Eqs. (17) and (18) where β is a parameter dependent on the pseudo mean flow profile, as suggested in [19]. This transformation is necessary to maintain linear stability of the PML equations. More discussions on

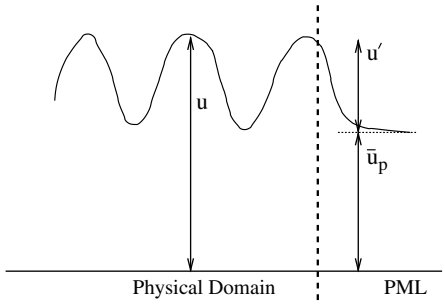

Fig. 2. Schematics of wave absorption in the PML domain.

parameter β and the pseudo mean flow will be given in the next section. Transformation (19) gives the following changes in partial derivatives, with respect to t and x,

$$\frac{\partial}{\partial t} \to \frac{\partial}{\partial \bar{t}}, \quad \frac{\partial}{\partial x} \to \frac{\partial}{\partial x} + \beta \frac{\partial}{\partial \bar{t}} \tag{20}$$

and (17) and (18) now become

$$\frac{\partial \mathbf{u}'}{\partial \bar{t}} + \beta \frac{\partial [\mathbf{F}_1 - \overline{\mathbf{F}}_1]}{\partial \bar{t}} + \frac{\partial [\mathbf{F}_1 - \overline{\mathbf{F}}_1]}{\partial x} + \frac{\partial [\mathbf{F}_2 - \overline{\mathbf{F}}_2]}{\partial y} + \frac{\partial [\mathbf{F}_3 - \overline{\mathbf{F}}_3]}{\partial z} = 0 \tag{21}$$

$$\mathbf{e}'_1 = \beta \frac{\partial [\mathbf{G} - \overline{\mathbf{G}}]}{\partial \bar{t}} + \frac{\partial [\mathbf{G} - \overline{\mathbf{G}}]}{\partial x}, \quad \mathbf{e}'_2 = \frac{\partial [\mathbf{G} - \overline{\mathbf{G}}]}{\partial y}, \quad \mathbf{e}'_3 = \frac{\partial [\mathbf{G} - \overline{\mathbf{G}}]}{\partial z} \tag{22}$$

In frequency domain, the above is

$$(-\mathrm{i}\bar{\omega}\tilde{\mathbf{u}}') + \beta(-\mathrm{i}\bar{\omega})\widetilde{[\mathbf{F}_1 - \overline{\mathbf{F}}_1]} + \frac{\partial \widetilde{[\mathbf{F}_1 - \overline{\mathbf{F}}_1]}}{\partial x} + \frac{\partial \widetilde{[\mathbf{F}_2 - \overline{\mathbf{F}}_2]}}{\partial y} + \frac{\partial \widetilde{[\mathbf{F}_3 - \overline{\mathbf{F}}_3]}}{\partial z} = 0 \tag{23}$$

$$\tilde{\mathbf{e}}'_1 = \beta(-\mathrm{i}\bar{\omega})\widetilde{[\mathbf{G} - \overline{\mathbf{G}}]} + \frac{\partial \widetilde{[\mathbf{G} - \overline{\mathbf{G}}]}}{\partial x}, \quad \tilde{\mathbf{e}}'_2 = \frac{\partial \widetilde{[\mathbf{G} - \overline{\mathbf{G}}]}}{\partial y}, \quad \tilde{\mathbf{e}}'_3 = \frac{\partial \widetilde{[\mathbf{G} - \overline{\mathbf{G}}]}}{\partial z} \tag{24}$$

where a tilde indicates the time Fourier transformed variable.

In the second step, we apply the PML complex change of variables to (23) and (24), which amounts to a modification of spatial derivatives as

$$\frac{\partial}{\partial x} \to \frac{1}{1 + \mathrm{i}\frac{\sigma_x}{\bar{\omega}}} \frac{\partial}{\partial x}, \quad \frac{\partial}{\partial y} \to \frac{1}{1 + \mathrm{i}\frac{\sigma_y}{\bar{\omega}}} \frac{\partial}{\partial y}, \quad \frac{\partial}{\partial z} \to \frac{1}{1 + \mathrm{i}\frac{\sigma_z}{\bar{\omega}}} \frac{\partial}{\partial z}$$

where σ_x, σ_y and σ_z are absorption coefficients, positive, and could be functions of x, y and z, respectively [6,7,19]. Application of the PML complex change of variables yields the following:

$$(-\mathrm{i}\bar{\omega}\tilde{\mathbf{u}}') + \beta(-\mathrm{i}\bar{\omega})\widetilde{[\mathbf{F}_1 - \overline{\mathbf{F}}_1]} + \frac{1}{1 + \frac{\mathrm{i}\sigma_x}{\bar{\omega}}} \frac{\partial \widetilde{[\mathbf{F}_1 - \overline{\mathbf{F}}_1]}}{\partial x} + \frac{1}{1 + \frac{\mathrm{i}\sigma_y}{\bar{\omega}}} \frac{\partial \widetilde{[\mathbf{F}_2 - \overline{\mathbf{F}}_2]}}{\partial y} + \frac{1}{1 + \frac{\mathrm{i}\sigma_z}{\bar{\omega}}} \frac{\partial \widetilde{[\mathbf{F}_3 - \overline{\mathbf{F}}_3]}}{\partial z} = 0 \tag{25}$$

$$\tilde{\mathbf{e}}'_1 = \beta(-\mathrm{i}\bar{\omega})\widetilde{[\mathbf{G} - \overline{\mathbf{G}}]} + \frac{1}{1 + \frac{\mathrm{i}\sigma_x}{\bar{\omega}}} \frac{\partial \widetilde{[\mathbf{G} - \overline{\mathbf{G}}]}}{\partial x}, \tilde{\mathbf{e}}'_2 = \frac{1}{1 + \frac{\mathrm{i}\sigma_y}{\bar{\omega}}} \frac{\partial \widetilde{[\mathbf{G} - \overline{\mathbf{G}}]}}{\partial y}, \tilde{\mathbf{e}}'_3 = \frac{1}{1 + \frac{\mathrm{i}\sigma_z}{\bar{\omega}}} \frac{\partial \widetilde{[\mathbf{G} - \overline{\mathbf{G}}]}}{\partial z} \tag{26}$$

In the third step, we try to re-write (25) and (26) in the time domain to obtain the absorbing boundary condition. This can be done in many different ways [20]. In order to keep the number of auxiliary variables small for the general three-dimensional equations considered here, we will use a "split" approach in the derivation below. Let

$$\mathbf{u}' = \mathbf{q}_1 + \mathbf{q}_2 + \mathbf{q}_3 \tag{27}$$

where $\mathbf{q}_1$, $\mathbf{q}_2$ and $\mathbf{q}_3$ are auxiliary variables that satisfy the following equations split from (25),

$$-\mathrm{i}\bar{\omega}\tilde{\mathbf{q}}_1 + \beta(-\mathrm{i}\bar{\omega})\widetilde{[\mathbf{F}_1 - \overline{\mathbf{F}}_1]} + \frac{1}{1 + \frac{\mathrm{i}\sigma_x}{\bar{\omega}}} \frac{\partial \widetilde{[\mathbf{F}_1 - \overline{\mathbf{F}}_1]}}{\partial x} = 0 \tag{28}$$

$$-\mathrm{i}\bar{\omega}\tilde{\mathbf{q}}_2 + \frac{1}{1 + \frac{\mathrm{i}\sigma_y}{\bar{\omega}}} \frac{\partial \widetilde{[\mathbf{F}_2 - \overline{\mathbf{F}}_2]}}{\partial y} = 0, -\mathrm{i}\bar{\omega}\tilde{\mathbf{q}}_3 + \frac{1}{1 + \frac{\mathrm{i}\sigma_z}{\bar{\omega}}} \frac{\partial \widetilde{[\mathbf{F}_3 - \overline{\mathbf{F}}_3]}}{\partial z} = 0 \tag{29}$$

We note that by adding the three equations in (28) and (29), we will recover (25). The auxiliary variables $\mathbf{q}_1$, $\mathbf{q}_2$ and $\mathbf{q}_3$ are introduced only to facilitate the conversion of Eq. (25) into one in the time domain.

By multiplying $\left(1 + \frac{\mathrm{i}\sigma_x}{\bar{\omega}}\right)$, $\left(1 + \frac{\mathrm{i}\sigma_y}{\bar{\omega}}\right)$ and $\left(1 + \frac{\mathrm{i}\sigma_z}{\bar{\omega}}\right)$ to the equations for $\tilde{\mathbf{q}}_1$ and $\tilde{\mathbf{e}}'_1$, $\tilde{\mathbf{q}}_2$ and $\tilde{\mathbf{e}}'_2$, and $\tilde{\mathbf{q}}_3$ and $\tilde{\mathbf{e}}'_3$, respectively, we get the following set of equations,

$$(-\mathrm{i}\bar{\omega}+\sigma_x)\tilde{\mathbf{q}}_1+\beta(-\mathrm{i}\bar{\omega}+\sigma_x)\widetilde{[\mathbf{F}_1-\overline{\mathbf{F}}_1]}+\frac{\partial\widetilde{[\mathbf{F}_1-\overline{\mathbf{F}}_1]}}{\partial x}=0 \tag{30}$$

$$(-\mathrm{i}\bar{\omega}+\sigma_y)\tilde{\mathbf{q}}_2+\frac{\partial\widetilde{[\mathbf{F}_2-\overline{\mathbf{F}}_2]}}{\partial y}=0,\quad (-\mathrm{i}\bar{\omega}+\sigma_z)\tilde{\mathbf{q}}_3+\frac{\partial\widetilde{[\mathbf{F}_3-\overline{\mathbf{F}}_3]}}{\partial z}=0 \tag{31}$$

$$\left(1+\frac{\mathrm{i}\sigma_x}{\bar{\omega}}\right)\tilde{\mathbf{e}}_1'=\beta(-\mathrm{i}\bar{\omega}+\sigma_x)\widetilde{[\mathbf{G}-\overline{\mathbf{G}}]}+\frac{\partial\widetilde{[\mathbf{G}-\overline{\mathbf{G}}]}}{\partial x} \tag{32}$$

$$\left(1+\frac{\mathrm{i}\sigma_y}{\bar{\omega}}\right)\mathbf{e}_2'=\frac{\partial\widetilde{[\mathbf{G}-\overline{\mathbf{G}}]}}{\partial y},\quad \left(1+\frac{\mathrm{i}\sigma_z}{\bar{\omega}}\right)\mathbf{e}_3'=\frac{\partial\widetilde{[\mathbf{G}-\overline{\mathbf{G}}]}}{\partial z} \tag{33}$$

We next write the time domain equations for the above as

$$\frac{\partial\mathbf{q}_1}{\partial\bar{t}}+\sigma_x\mathbf{q}_1+\beta\sigma_x[\mathbf{F}_1-\overline{\mathbf{F}}_1]+\beta\frac{\partial[\mathbf{F}_1-\overline{\mathbf{F}}_1]}{\partial\bar{t}}+\frac{\partial[\mathbf{F}_1-\overline{\mathbf{F}}_1]}{\partial x}=0 \tag{34}$$

$$\frac{\partial\mathbf{q}_2}{\partial\bar{t}}+\sigma_y\mathbf{q}_2+\frac{\partial[\mathbf{F}_2-\overline{\mathbf{F}}_2]}{\partial y}=0,\quad \frac{\partial\mathbf{q}_3}{\partial\bar{t}}+\sigma_z\mathbf{q}_3+\frac{\partial[\mathbf{F}_3-\overline{\mathbf{F}}_3]}{\partial z}=0 \tag{35}$$

$$\mathbf{e}_1'+\sigma_x\mathbf{r}_1=\beta\sigma_x[\mathbf{G}-\overline{\mathbf{G}}]+\beta\frac{\partial[\mathbf{G}-\overline{\mathbf{G}}]}{\partial\bar{t}}+\frac{\partial[\mathbf{G}-\overline{\mathbf{G}}]}{\partial x} \tag{36}$$

$$\mathbf{e}_2'+\sigma_y\mathbf{r}_2=\frac{\partial[\mathbf{G}-\overline{\mathbf{G}}]}{\partial y},\quad \mathbf{e}_3'+\sigma_z\mathbf{r}_3=\frac{\partial[\mathbf{G}-\overline{\mathbf{G}}]}{\partial z} \tag{37}$$

where a second set of auxiliary variables $\mathbf{r}_1$, $\mathbf{r}_2$, $\mathbf{r}_3$ are defined as

$$\frac{\partial\mathbf{r}_i}{\partial\bar{t}}=\mathbf{e}_i',\quad i=1,2,3$$

Finally, by writing back in the original space and time variables, we obtain the time-domain absorbing boundary equations as follows,

$$\frac{\partial\mathbf{u}}{\partial t}+\frac{\partial[\mathbf{F}_1-\overline{\mathbf{F}}_1]}{\partial x}+\frac{\partial[\mathbf{F}_2-\overline{\mathbf{F}}_2]}{\partial y}+\frac{\partial[\mathbf{F}_3-\overline{\mathbf{F}}_3]}{\partial z}+\sigma_x\mathbf{q}_1+\sigma_y\mathbf{q}_2+\sigma_z\mathbf{q}_z+\beta\sigma_x[\mathbf{F}_1-\overline{\mathbf{F}}_1]=0 \tag{38}$$

$$\frac{\partial\mathbf{q}_1}{\partial t}+\sigma_x\mathbf{q}_1+\frac{\partial[\mathbf{F}_1-\overline{\mathbf{F}}_1]}{\partial x}+\beta\sigma_x[\mathbf{F}_1-\overline{\mathbf{F}}_1]=0 \tag{39}$$

$$\frac{\partial\mathbf{q}_2}{\partial t}+\sigma_y\mathbf{q}_2+\frac{\partial[\mathbf{F}_2-\overline{\mathbf{F}}_2]}{\partial y}=0 \tag{40}$$

$$\frac{\partial\mathbf{q}_3}{\partial t}+\sigma_z\mathbf{q}_3+\frac{\partial[\mathbf{F}_3-\overline{\mathbf{F}}_3]}{\partial z}=0 \tag{41}$$

$$\frac{\partial\mathbf{r}_1}{\partial t}+\sigma_x\mathbf{r}_1=\frac{\partial[\mathbf{G}-\overline{\mathbf{G}}]}{\partial x}+\beta\sigma_x[\mathbf{G}-\overline{\mathbf{G}}] \tag{42}$$

$$\frac{\partial\mathbf{r}_2}{\partial t}+\sigma_y\mathbf{r}_2=\frac{\partial[\mathbf{G}-\overline{\mathbf{G}}]}{\partial y} \tag{43}$$

$$\frac{\partial\mathbf{r}_3}{\partial t}+\sigma_z\mathbf{r}_3=\frac{\partial[\mathbf{G}-\overline{\mathbf{G}}]}{\partial z} \tag{44}$$

where $\mathbf{F}_i$ and $\mathbf{G}$ are functions of $\mathbf{u}$ and $\mathbf{e}_i$, $i=1,2,3$, as defined by (3)–(5) and (11), and $\mathbf{e}_i$ are computed by

$$\mathbf{e}_1=\frac{\partial\mathbf{G}}{\partial x}-\sigma_x\mathbf{r}_1+\beta\sigma_x[\mathbf{G}-\overline{\mathbf{G}}] \tag{45}$$

$$\mathbf{e}_2=\frac{\partial\mathbf{G}}{\partial y}-\sigma_y\mathbf{r}_2 \tag{46}$$

$$\mathbf{e}_3=\frac{\partial\mathbf{G}}{\partial z}-\sigma_z\mathbf{r}_3 \tag{47}$$

(38)–(44) are the governing equations to be solved in the PML domain. We should point out that, when the flux vectors are nonlinear functions, unlike in linear cases, the time domain equations (34)–(37) are no longer the exact inverse Fourier transformation of the frequency domain equations (30)–(33). As a result, Eqs. (38)–(44) are not deemed formally perfectly matched to the nonlinear governing equation (1), although numerical results are still quite satisfactory as we will demonstrate later in the paper.

We note that Eq. (38) is equivalent to the sum of Eqs. (39)–(41) and thus is not formally an independent equation, because the following relation holds true in the PML domain,

$$\mathbf{u} = \bar{\mathbf{u}}_p + \mathbf{q}_1 + \mathbf{q}_2 + \mathbf{q}_3 \tag{48}$$

However, Eq. (38) can often be implemented easily as it is written in the original physical variables. The use of (38) will also reduce the requirement on storage, because an inspection of Eqs. (38)–(44) shows that not all the auxiliary variables are needed everywhere inside the PML domain. The auxiliary variables are only needed where the corresponding absorption coefficient is non-zero. For instance, $\mathbf{q}_1$ and $\mathbf{r}_1$ are only necessary at x-layers where σ_x is not zero; similarly, $\mathbf{q}_2$, $\mathbf{r}_2$ and $\mathbf{q}_3$, $\mathbf{r}_3$ are only necessary where σ_y and σ_z are respectively not zero. Since absorption coefficients σ_x, σ_y and σ_z are functions of x, y or z, respectively, regions of non-zero absorption coefficients, as well as the required auxiliary variables, are as shown in Fig. 3 for a section of computational domain with PML.

Therefore, the equations to be solved in a PML domain will be (38), for $\mathbf{u}$, plus additional equations from (39)–(44) for the auxiliary variables $\mathbf{q}_i$ and $\mathbf{r}_i$ wherever the corresponding absorption coefficient is non-zero. At the corner layer where all the absorption coefficients are non-zero, the equation for one of the $\mathbf{q}$ variables may be substituted by relation (48) if so desired.

We also note that, the three terms involving spatial derivatives of $\overline{\mathbf{F}}_1$, $\overline{\mathbf{F}}_2$ and $\overline{\mathbf{F}}_3$ can obviously be dropped from (38) if the pseudo mean flow satisfies the steady state equation (16). However, the equations as written in (38)–(43) would still be self-consistent in the limit of $\mathbf{u} \to \bar{\mathbf{u}}_p$ even if the pseudo mean flow $\bar{\mathbf{u}}_p$, $\bar{\mathbf{e}}_1$, $\bar{\mathbf{e}}_2$ and $\bar{\mathbf{e}}_3$ do not exactly satisfy (16). That is, $\mathbf{u} = \bar{\mathbf{u}}_p$ with $\mathbf{q}_i = \mathbf{r}_i = 0$ will always satisfy the equations written as (38)–(43). This could be helpful for problems where only a pseudo mean flow that approximately satisfies the steady state equation (16) would be available. For such cases, inclusion of the flux expressions from the pseudo mean flow as written in (38) can prove to be useful.

The equations given above, (38)–(44), include the PML for the inviscid nonlinear Euler equations as a special case, by neglecting the viscous terms. Exclusion of viscous effects leads to the elimination of terms involving $\mathbf{e}_1$, $\mathbf{e}_2$ and $\mathbf{e}_3$ and, consequently, the necessity for auxiliary variables $\mathbf{r}_1$, $\mathbf{r}_2$ and $\mathbf{r}_3$. Thus, the equations to be solved in the absorbing zone for inviscid problems will be (38)–(41).

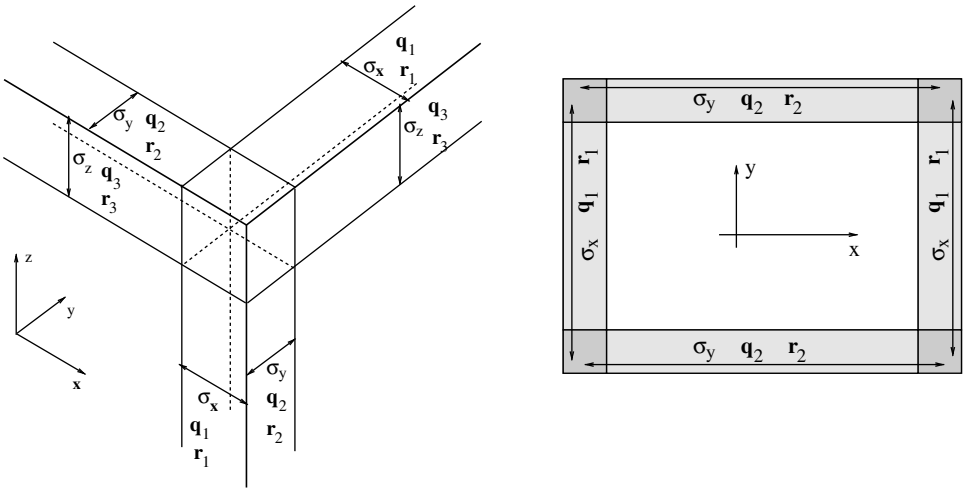

Fig. 3. Schematics of physical and PML domains. The sub-domains where the absorption coefficients are non-zero are indicated by arrows. Left: a section of 3D domain; Right: a 2D domain layout.

3. Pseudo mean flow and value for β

In our derivation above, the only requirement on the pseudo mean flow $\bar{\mathbf{u}}_p$ is that it would satisfy the steady state equation (16). As pointed out earlier, the exact mean flow is often unknown at the start of a computation. A suitable known solution to the steady equation (16) that resembles the actual flow can be a viable pseudo mean flow in the formulation of the PML equation. In this sense, the choice of pseudo mean flow is not unique. For many practical problems, such a pseudo mean flow would be relatively easy to find [17,21]. For instance, a parallel flow will satisfy the steady state Euler equation and thus can be used as a pseudo mean flow for the appropriate nonlinear Euler simulations. For example, in primitive variables,

$$\begin{bmatrix} \rho \\ u \\ v \\ w \\ p \end{bmatrix} = \begin{bmatrix} \bar{\rho}_p(y) \\ \bar{u}_p(y) \\ 0 \\ 0 \\ \bar{p}_p \end{bmatrix} \tag{49}$$

will satisfy (16) without the viscous terms, where $\bar{\rho}_p(y)$ and $\bar{u}_p(y)$ can be freely adjusted to resemble the flow at the non-reflecting boundary. Likewise, a constant uniform mean flow also satisfies the steady state Navier–Stokes equations.

Once the pseudo mean flow is chosen, the parameter β in the PML equations is to be determined as described in [19]. The purpose of the space–time transformation given in (19) is to ensure linear stability of the PML equations. It is used to correct the inconsistency in the phase and group velocities of the acoustic wave modes in the derivation process.

For inviscid problems, since the linearization of PML equations derived in this paper is equivalent to the linearized Euler equation given in [19] in frequency domain, the value for β can be found in the same way as that described in [19] based on the pseudo mean flow employed. In general, a study on the dispersion relation $D(\omega, k) = 0$ for the linear waves supported by the pseudo mean flow would be required to determine the value of β. For the special case where the density of the pseudo mean flow is constant, i.e., $\bar{\rho}_p(y) = 1$, we may use a simple empirical formula given in [19],

$$\beta = \frac{\overline{U}_m}{1 - \overline{U}_m^2}, \quad \overline{U}_m = \frac{1}{b-a}\int_a^b \bar{u}_p(y)\mathrm{d}y \tag{50}$$

where the computational domain for y is $[a, b]$.

For viscous problems, it has been found that the presence of viscosity will not substantially affect the value for β, since the inconsistency in the phase and group velocities occurs only for the acoustic waves for a parallel flow in the direction of x, to which viscous effects are usually small. As an example, we consider a pseudo mean flow given by

$$\bar{u}_p(y) = \frac{1}{2}(u_1 + u_2) + \frac{1}{2}(u_1 - u_2)\tanh\left(\frac{y}{0.2}\right), \quad \bar{v}_p = 0, \quad \bar{\rho}_p(y) = 1, \quad \bar{p}_p = \frac{1}{\gamma}$$

with

$$u_1 = 0.8, \quad u_2 = 0.2, \quad \text{and} \quad -1 \leqslant y \leqslant 1$$

A numerical study of the dispersion relations of linear waves gives the following values for β:

$$\text{Inviscid} : \beta \approx 0.63$$
$$\mathrm{Re} = 5000 : \beta \approx 0.63$$
$$\mathrm{Re} = 500 : \beta \approx 0.63$$
$$\mathrm{Re} = 50 : \beta \approx 0.64$$

while the empirical formula (50) gives $\beta \approx U_m/(1 - U_m^2) = 2/3 \approx 0.67$ by using $U_m = 1/2$, the average of $\bar{u}_p$.

4. Numerical examples

In this section, we present numerical examples of using the absorbing boundary conditions derived in the present study for the nonlinear Euler and Navier–Stokes equations, based on a viscous computational aeroacoustic approach [23,22]. The dispersion-relation-preserving scheme [26] is applied for spatial discretization and the optimized 5- and 6-stage alternating low-dissipation and low-dispersion Runge–Kutta scheme [15] is used for time integration.

4.1. Isentropic vortex using nonlinear Euler equations

We first present a numerical example that verifies the effectiveness of the PML for the nonlinear Euler equation. The two-dimensional nonlinear Euler equations support an advective solution of the form

$$\begin{pmatrix} \rho(\mathbf{x},t) \\ u(\mathbf{x},t) \\ v(\mathbf{x},t) \\ p(\mathbf{x},t) \end{pmatrix} = \begin{pmatrix} 0 \\ U_0 \\ V_0 \\ 0 \end{pmatrix} + \begin{pmatrix} \rho_r(r) \\ -u_r(r)\sin\theta \\ u_r(r)\cos\theta \\ p_r(r) \end{pmatrix} \tag{51}$$

where $r = \sqrt{(x-U_0t)^2 + (y-V_0t)^2}$. For any given $u_r(r)$ and $\rho_r(r)$, the pressure $p_r(r)$ is found by

$$\frac{\mathrm{d}}{\mathrm{d}r}p_r(r) = \rho_r(r)\frac{u_r^2(r)}{r} \tag{52}$$

Eq. (51) gives a solution that advects with constant velocity (U_0, V_0).

For our numerical tests, we consider a velocity distribution of the form

$$u_r(r) = \frac{U'_{\max}}{b} r\, \mathrm{e}^{\frac{1}{2}\left(1-\frac{r^2}{b^2}\right)} \tag{53}$$

where $U'_{\max}$ is the maximum velocity at $r = b$. For isentropic flow, we assume

$$p_r = \frac{1}{\gamma}\rho_r^{\gamma} \tag{54}$$

and, by integrating (52), we get the following density and pressure distributions,

$$\rho_r(r) = \left(1 - \frac{1}{2}(\gamma-1)U'^2_{\max}\,\mathrm{e}^{1-\frac{r^2}{b^2}}\right)^{1/(\gamma-1)} \tag{55}$$

$$p_r(r) = \frac{1}{\gamma}\left(1 - \frac{1}{2}(\gamma-1)U'^2_{\max}\,\mathrm{e}^{1-\frac{r^2}{b^2}}\right)^{\gamma/(\gamma-1)} \tag{56}$$

The v-velocity contours of a numerical solution is shown in Fig. 4. The initial condition is that given in (51) with $(U_0, V_0) = (0.5, 0)$, $U'_{\max} = 0.5U_0 = 0.25$, and $b = 0.2$. The nonlinear Euler equation is solved by a finite difference scheme in a computational domain of $[-1.2, 1.2] \times [-1.2, 1.2]$ with a uniform grid of $\Delta x = \Delta y = 0.02$, including the surrounding PML domain of 10 grid points in width. In particular, the PML absorption coefficient is taken to be

$$\sigma_x = \sigma_{\max}\left|\frac{x-x_0}{D}\right|^{\alpha}$$

with $\sigma_{\max} = 20$, $\alpha = 4$ and x_0 is the location of interface between PML and physical domains. A similar model for σ_y is used. A grid stretching in the PML domain is also used to increase the efficiency of the absorbing zone [28]. The stretching factor is

$$\alpha(x) = 1 + 2\left|\frac{x-x_0}{D}\right|^2$$

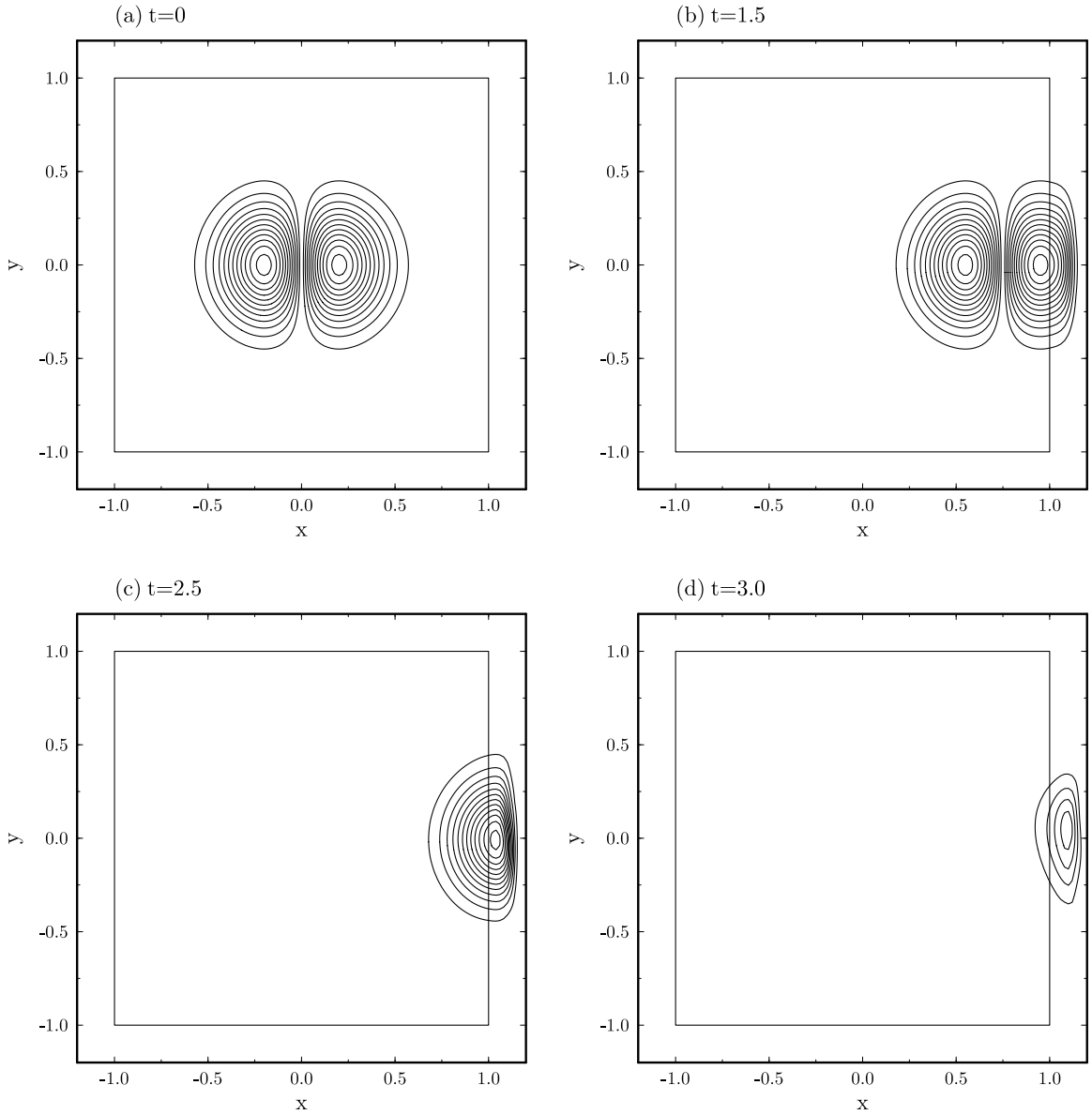

Fig. 4. v-Velocity contour levels from ± 0.02 to ± 0.24.

as noted in [19]. The pseudo mean flow is taken to be the same as the uniform background flow with parameter $\beta = U_0/(1 - U_0^2)$.

Fig. 4 shows the v-velocity contours at time $t = 0$, 1.5, 2.5 and 3.5, respectively, at levels from ± 0.02 to ± 0.4. Absorption of the vortex by PML at the outflow boundary is clearly demonstrated. Fig. 5 shows the v-velocity as a function of x along $y = 0$, as the vortex exits the computational domain. Also plotted in dashed lines are the exact solution. The numerical solution matches the exact solution in the Euler domain while decays exponentially in the PML domain.

To further assess the magnitude of reflection error, Fig. 6 plots the maximum difference between the numerical solution and a reference solution obtained using a larger computational domain, along a vertical line near the outflow boundary, as a function of time. The reflection errors are indeed quite small and decrease with an increase in the width of the PML domain employed. Fig. 7 shows the trend in the reduction of the maximum reflection error, for the v-velocity component as well as the pressure, as the PML width increases.

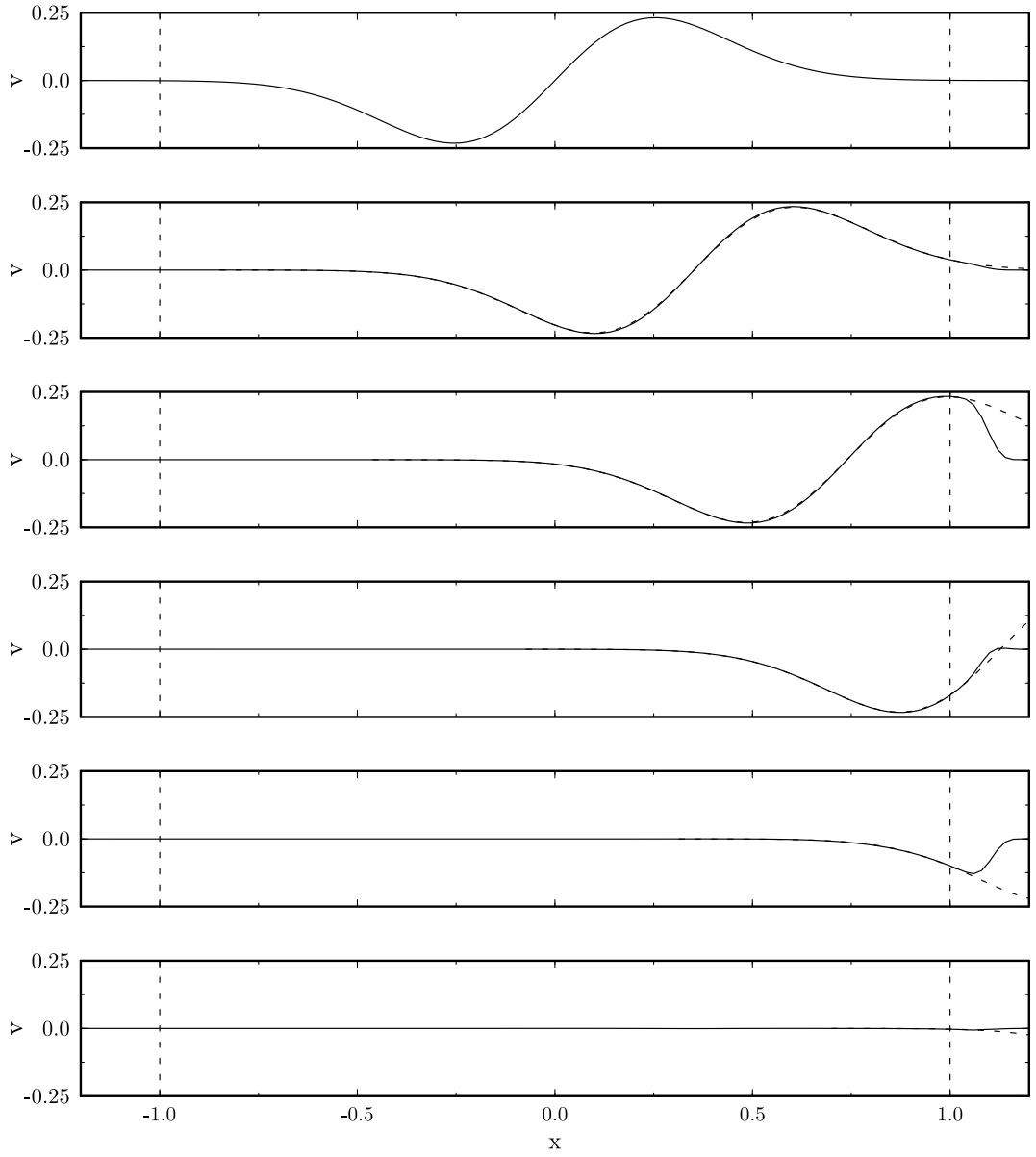

Fig. 5. v-velocity profile along $y = 0$ at progressive time frames. Solid line: numerical solution; dashed line: exact solution. Vertical dashed lines indicate the Euler/PML interface.

Fig. 8 shows the maximum reflection error in v-velocity component relative to the maximum velocity of the vortex $U'_{\max}$ along $x = 0.9$ near the outflow boundary for various strengths of the vortex. Although reflection error generally increases with the strength of the vortex, a relative error of less than 1% is achieved for all cases with PML width of 20 grid points. Fig. 9 plots the maximum reflection error, for the v-velocity component and the pressure, as a function of the vortex strength $U'_{\max}/U_0$ in a log scale, showing the trend of increase in reflection error with the increase in the nonlinearity.

4.2. Isentropic vortex with nonlinear Navier–Stokes equations

The example in the previous section is repeated using the nonlinear Navier–Stokes equations. The computational domain and initial condition are similar but viscous terms in the governing equations are now

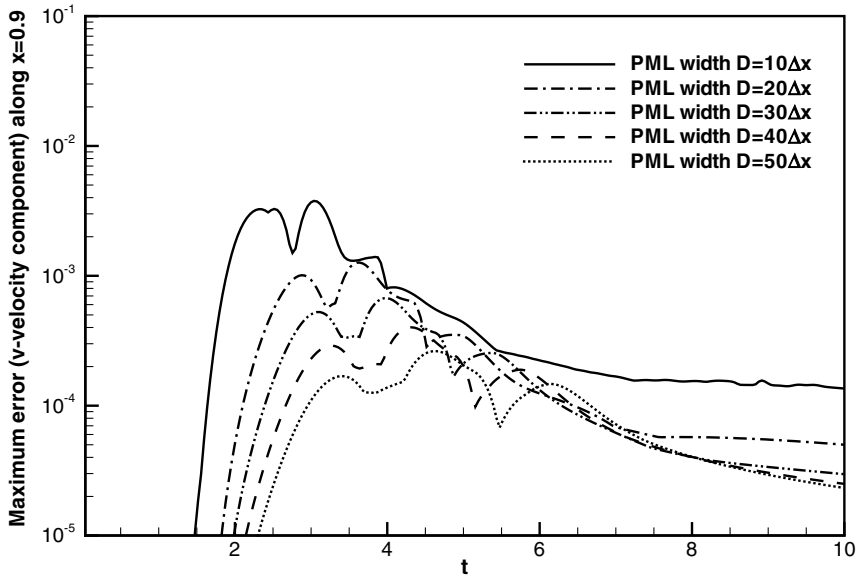

Fig. 6. Maximum reflection error (v-velocity component) along $x = 0.9$ near the outflow boundary. PML width is as indicated.

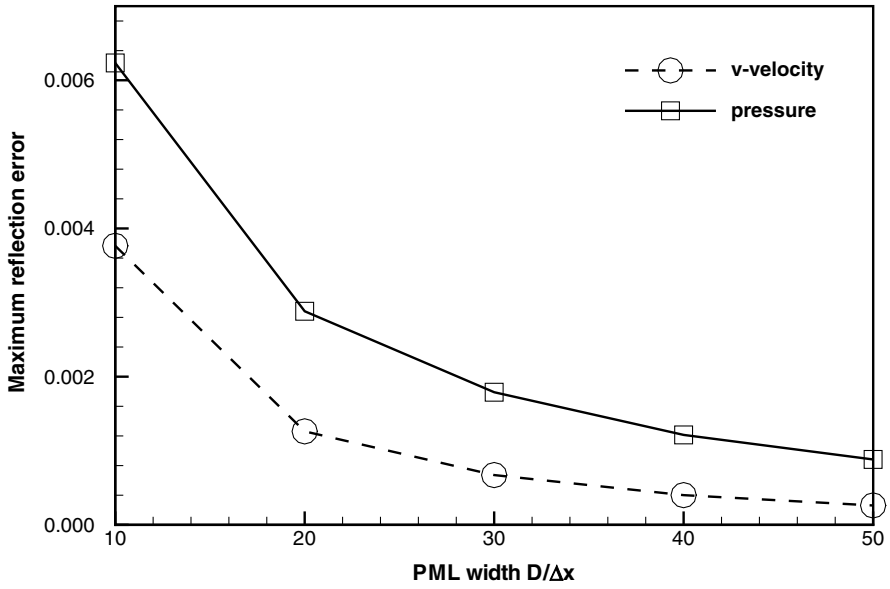

Fig. 7. Maximum reflection error, for the v-velocity component and pressure, as a function of the PML width D.

included. The numerical solution is compared with a large domain solution to obtain a measure of the reflection error. Fig. 10 shows the reflection error for the v-velocity component relative to the maximum perturbation velocity $U'_{\max}$ of the initial vortex, at various Reynolds numbers which is based on the velocity U_0. Fig. 11 shows the reflection error for the pressure relative to the maximum pressure perturbation caused by the vortex, $P'_{\max}$, which is defined by $|p_r(0) - p_r(\infty)| \approx \frac{1}{2} U'^2_{\max}$ as given in (56). It is seen that generally reflection errors shown in Figs. 10 and 11 decrease with the Reynolds number. This reduction in reflection error is partly due to a weakening of vortex by viscous diffusion effect when it reaches the outflow boundary from its initial position $(x, y) = (0, 0)$. Fig. 12 shows the trend of reduction of the maximum reflection error as a function of the Reynolds number.

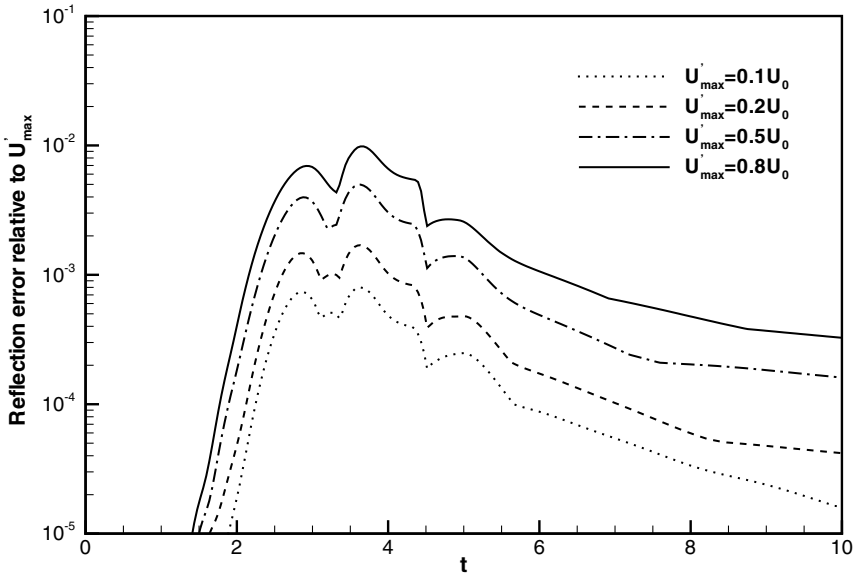

Fig. 8. Maximum relative reflection error (v-velocity component) along $x = 0.9$ near the outflow boundary. PML width $D = 20\Delta x$.

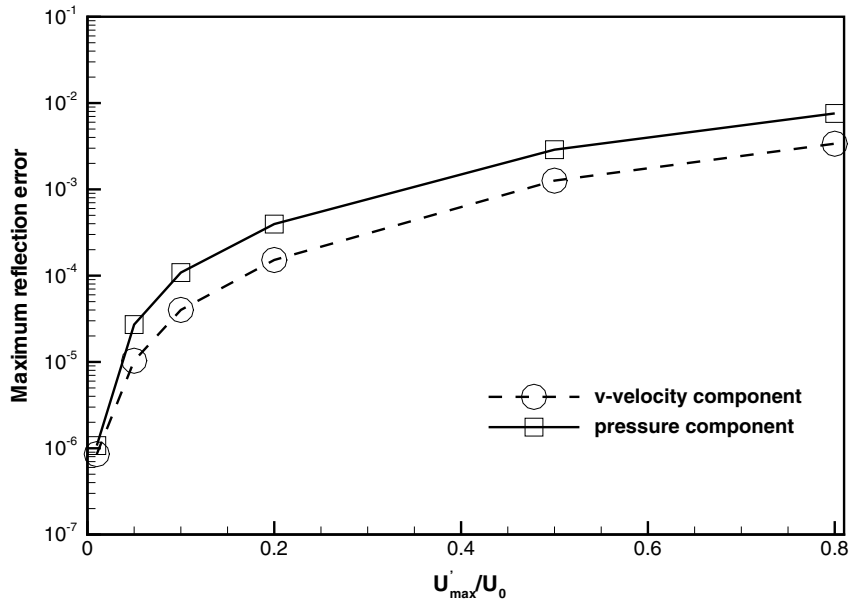

Fig. 9. Maximum reflection error, for the v-velocity component and the pressure, as a function of vortex strength $U'_{\max}/U_0$.

Fig. 13 shows the effect of the strength of vortex on the reflection errors in the Navier–Stokes simulation. In this example, the background uniform flow is taken to be $U_0 = 0.2$ while the maximum velocity of the vortex perturbation is increased from $U'_{\max} = 0.1U_0$ up to $2.0U_0$, a very high nonlinearity. It is observed that reflection errors increase with the strength of the vortex. This is not unexpected because the nonlinearity increases with $U'_{\max}$. In particular, we note that when $U'_{\max}$ is greater than U_0, part of the vortex region actually have a total velocity in direction opposite to the background mean flow.

Fig. 14 shows the effects of the mean flow Mach number on the effectiveness of the PML domain. The background flow Mach number U_0 is varied from 0.2 to 0.8 while the strength of vortex $U'_{\max}$ is kept as $0.5U_0$ in

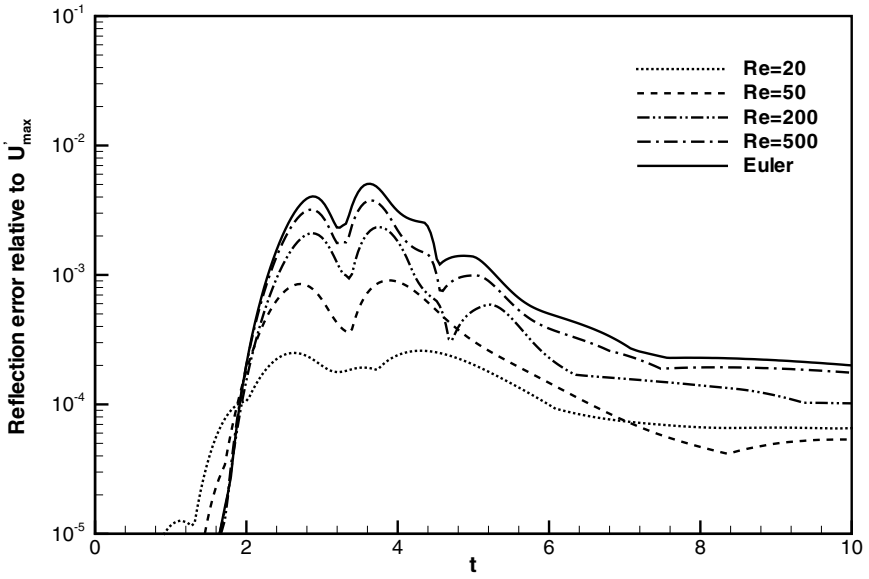

Fig. 10. Maximum relative reflection error (v-velocity component) at various Reynolds numbers. $U_0 = 0.5$, $U'_{\max} = 0.5U_0$.

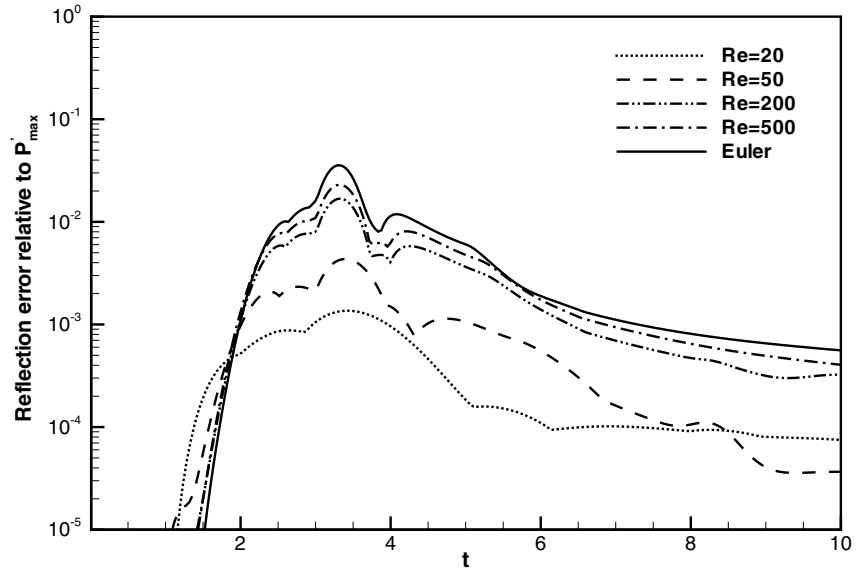

Fig. 11. Maximum relative reflection error (pressure) at various Reynolds numbers. $U_0 = 0.5$, $U'_{\max} = 0.5U_0$.

each case. The maximum reflection errors are found to be of similar magnitude. This means that the effectiveness of the absorbing boundary condition does not strongly depend on the mean flow Mach number.

4.3. Viscous flow over a circular cylinder

In this example, we show the absorption of nonlinear vortices shedded by a viscous flow over a circular cylinder. The uniform incoming flow has a Mach number $M = U_\infty/a_\infty = 0.2$. Here U_∞ and a_∞ denote the velocity of the uniform flow and the speed of sound, respectively. The velocity and the length are nondimensionalized by a_∞ and the diameter of the cylinder d, respectively. The Reynolds number is defined as

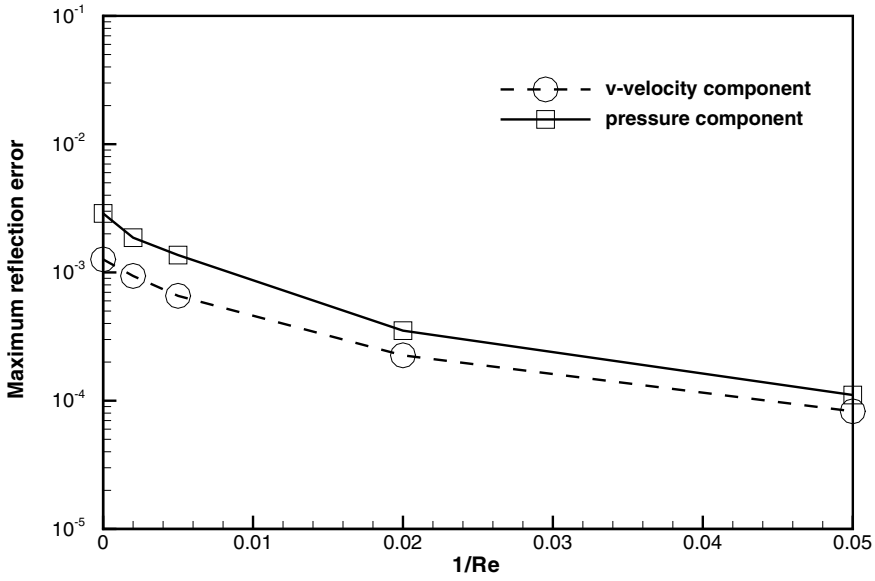

Fig. 12. Maximum relative reflection error, for the v-velocity and pressure, as a function of 1/Re.

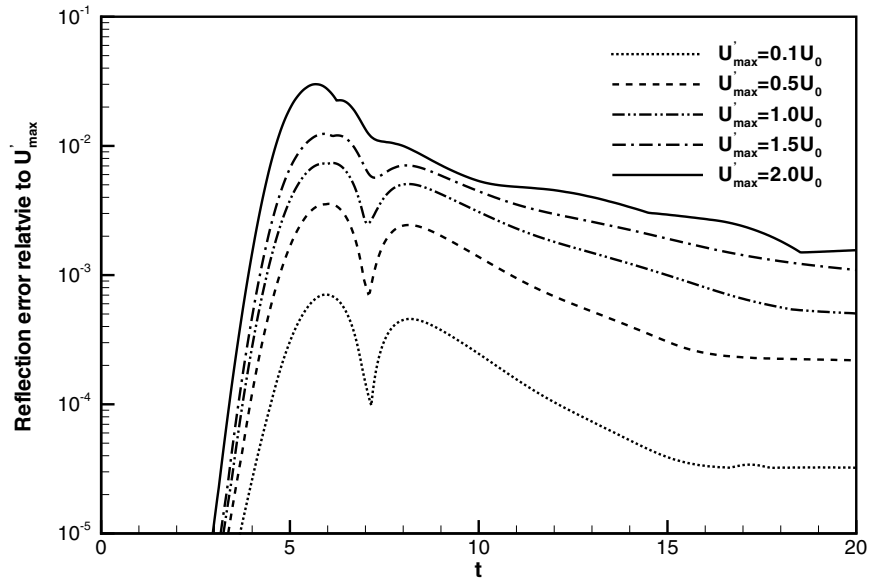

Fig. 13. Maximum relative reflection error for various strengths of the vortex. $U_0 = 0.2$, $Re = 200$.

$Re = U_\infty d/v_\infty$, where v_∞ is the reference kinematic viscosity. For the present calculation, $Re = 150$ and the Prandtl number $Pr = 0.75$.

Fig. 15 shows the multi-domain computational mesh layout with overset grids, for $(x, y) \in [-7, 11] \times [-7, 7]$. The cylinder is located at $(x, y) = (0, 0)$ with a radius of 0.5 and all PML domains have a width of 20 grid points. The main computational domain is divided into two regions. An O-grid system with non-uniform meshes is adopted around the cylinder, covering a region in polar coordinates of $0.5 \leqslant r \leqslant 1.5$, $0 \leqslant \theta \leqslant 2\pi$, with a non-uniform grid spacing of $\Delta r_{\min} = 0.005$, $\Delta r_{\max} = 0.02$, and $\Delta\theta = 1.2^o$. Another region is composed of multi-block uniform meshes with $\Delta x = \Delta y = \Delta$. In each block, the value of Δ is specified in Fig. 15. A high-order Lagrange interpolation technique is utilized for the overset grids.

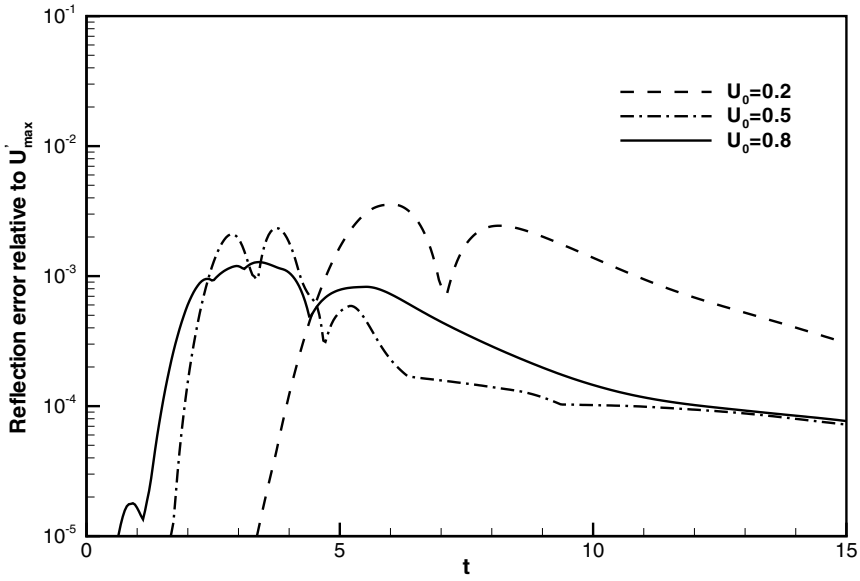

Fig. 14. Maximum relative reflection error for different mean flows. $U'_{\max} = 0.5U_0$, $Re = 200$.

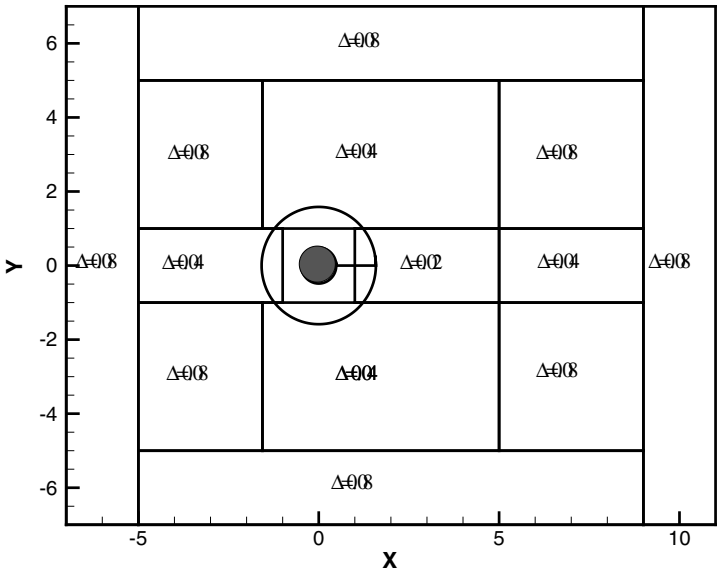

Fig. 15. Mesh and computational domain (global).

Calculation is initiated with the uniform flow for the entire computational domain. A natural choice for the pseudo mean flow is the incoming uniform flow at all four PML domains, namely,

$$\bar{u}_{\mathrm{p}} = M, \quad \bar{v}_{\mathrm{p}} = 0, \quad \bar{\rho}_{\mathrm{p}} = 1, \quad \bar{p}_{\mathrm{p}} = 1/\gamma \tag{57}$$

with $\beta = M/(1 - M^2)$. Fig. 16 shows the instantaneous pressure contours at $t = 5, 8, 10$ and 450, calculated by the direct numerical simulation, solving (1) in the physical domain and PML equations (38)–(44) in the absorbing zones. The initial transient pressure wave exits the computational domain without noticeable reflection. After $t = 400$, vortex shedding is observed. Fig. 17 shows the vorticity contours over a period of vortex shedding. The absorption of the nonlinear vortices by the PML zone at the outflow is clearly seen.

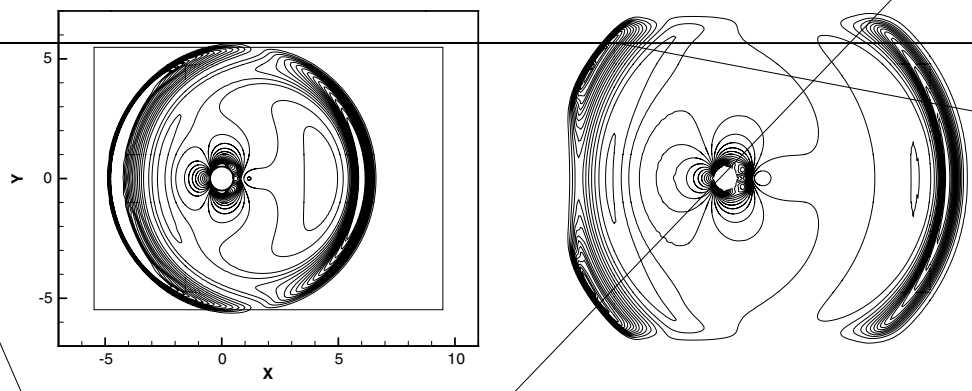

In Fig. 18, we show the v-velocity and pressure at a point $(x, y) = (9, 0)$ on the outflow boundary of the physical domain as a function of time, from $t = 0$ to $t = 700$. Also plotted, in symbols, is the result of a reference solution computed using a larger computational domain. The reference solution is obtained using a computational domain of $[-7, 30] \times [-7, 7]$. The discrepancy seen in the pressure around time $t = 300$ is due to the truncation of the initial wake flow by the smaller computational domain before the periodic vortex shedding is started. Good agreement in the time history of the periodically shed vortices is observed. Figs. 17 and 18 indicate that the PML domain at the outflow boundary can effectively absorb these vortices as they convect out of the computational domain.

4.4. Shear layer roll-up vortices

In this example, we simulate a mixing layer with roll-up vortices induced by the Kelvin–Helmholtz instability. The PML equations developed in the present paper are applied as the absorbing boundary condition. The Navier–Stokes equation (1) is solved in a computational domain of $[-1, 9] \times [-1, 1]$ by a finite difference scheme, with $\Delta x = 0.05$ and $\Delta y = 0.01$. The Reynolds number for this computation is 10,000. PML domain with a width of 10 grid points are added at four sides of the computational domain to absorb all out-going waves. The initial condition is

$$\begin{pmatrix} \rho \\ u \\ v \\ p \end{pmatrix} = \begin{pmatrix} \bar{\rho}(y) \\ \overline{U}(y) \\ 0 \\ \frac{1}{\gamma} \end{pmatrix} \tag{58}$$

where

$$\overline{U}(y) = \frac{1}{2}\left[(U_1 + U_2) + (U_1 - U_2)\tanh\left(\frac{2y}{\delta}\right)\right], \quad \bar{\rho}(y) = \frac{1}{\overline{T}(y)} \tag{59}$$

with

$$\overline{T}(y) = T_1\frac{\overline{U} - U_2}{U_1 - U_2} + T_2\frac{U_1 - \overline{U}}{U_1 - U_2} + \frac{\gamma - 1}{2}(U_1 - \overline{U})(\overline{U} - U_2) \tag{60}$$

where the mean temperature $\overline{T}(y)$ is determined by the Crocco relation for compressible flows. The parameters are

$$U_1 = 0.8, \quad U_2 = 0.2, \quad \delta = 0.4, \quad T_1 = 1, \quad T_2 = 0.8, \quad \gamma = 1.4.$$

A source term is added to the energy equation in (1) to induce the instability wave. The source term is of the form

$$s(x, y, t) = 5\sin(\omega t)\,\mathrm{e}^{-(\ln 2)[(x-x_0)^2+(y-y_0)^2]/r_0^2}$$

where $\omega = \pi/2$, $(x_0, y_0) = (-0.5, 0)$ and $r_0 = 0.03$.

The added source term excites the Kelvin–Helmholtz instability wave which would grow exponentially and develop into roll-up vortices. Fig. 19 gives a time sequence of vorticity contours showing the absorption of out-going vorticities at the outflow boundary. Fig. 20 plots the time history of v-velocity and pressure at a point close to the outflow boundary. Also plotted in symbols are the corresponding time histories from a large domain calculation whose solution is not affected by the boundary. Very good agreement is found.

For the calculation shown in Fig. 19, the pseudo mean flow $\bar{u}_p$ used in the PML equation is the same parallel flow as that of the initial condition (58), with a value of $\beta = 1/1.4$ according to the linear wave analysis given in [19]. Calculations have also been made using different pseudo mean flow profiles to study the effects of pseudo mean flow choices on the accuracy of the absorbing boundary condition. In particular, three different pseudo mean flows have been applied at the outflow boundary where the thickness parameter for the

u-velocity profile is taken to be $\delta = 0.4, 0.6$ and 0.8, respectively. Fig. 21 shows the instantaneous u-velocity contours for the three cases. The velocity contours inside the physical domain are nearly identical in the three cases. This indicates that the PML equation is relatively accommodating in the choice of pseudo mean flow as long as it is reasonably close to the actual flow.

4.5. Flat-plate boundary layer

In this example, we apply the PML absorbing boundary condition to the computation of steady boundary layer profile formed by a uniform flow over a flat plate. A schematic of the computational domain is shown in Fig. 22. The incoming flow is uniform in the direction of x-axis with Mach number $M = 0.1$. The Reynolds number is $Re = 10{,}000$ and the Prandtl number $Pr = 0.708$.

PML domains are used at all the three non-reflecting boundaries. For the left inflow and top radiation boundaries, the pseudo mean flow is the same as the incoming uniform flow. For the PML at the outflow boundary, in order to adjust for the no-slip boundary condition at the wall, the pseudo mean flow is taken to be the following,

$$\bar{u}_{\mathrm{p}} = \begin{cases} M & y > \delta \\ M \sin(\pi y/2\delta) & 0 \leqslant y \leqslant \delta \end{cases} \tag{61}$$

$$\bar{v}_{\mathrm{p}} = 0, \quad \bar{p}_{\mathrm{p}} = \frac{1}{\gamma}, \quad \bar{\rho}_{\mathrm{p}} = \frac{1 + 0.5(\gamma - 1)\bar{u}_{\mathrm{p}}^2}{1 + 0.5(\gamma - 1)M^2} \tag{62}$$

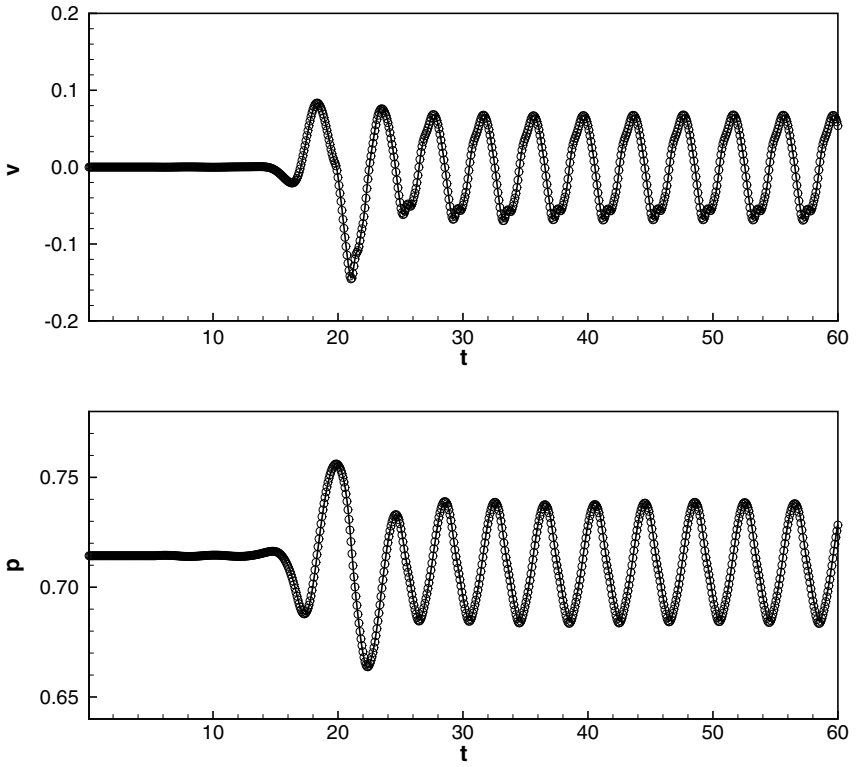

Fig. 20. Time history of the v-velocity and pressure. Solid line: computational; circle: large domain calculation.

The thickness parameter δ in (61) is taken to be an estimated boundary layer thickness. For the present Reynolds number, $\delta = 0.053$ is used in the computation. The value of β is 0.0911 obtained by the formula given in (50).

Numerical calculation starts with an initialization of all variables in the physical domain by the uniform incoming flow. After the transients are absorbed by the PML domains, the numerical solution approaches to a steady state. Fig. 23 shows the time history of the residues of the steady state governing equations in the physical domain. The L2 norm of the residues eventually becomes less than 10^{-8}, an indication that the numerical solution is close to the steady state solution. Fig. 24 shows the contours of the u-velocity in the whole computational domain and Fig. 25 shows the normalized stream-wise velocity profile. Also plotted in Fig. 25 are the theoretical Blasius similarity solution, with good agreement. We note that the PML has been primarily designed to absorb time-dependent out-going waves. The purpose of this example is to demonstrate the possibility of using the proposed absorbing boundary condition for steady state applications. Further studies on the efficiency of PML for such calculations will be carried out in the future.

We also note that the pseudo mean flow (61) used in the outflow PML domain does not exactly satisfy the steady state Navier–Stokes equations. Nonetheless, as pointed out earlier in Section 3, the equations written in the form of (38)–(44) still appear to be effective. For steady state computations, it is also possible to update the initial pseudo mean flow with an improved mean flow as the computation proceeds.

4.6. Three-dimensional acoustic pulse

In this example, the propagation of a three-dimensional nonlinear acoustic pulse in a uniform mean flow is simulated using the nonlinear Navier–Stokes equations. The PML absorbing boundary conditions are applied in all non-reflecting boundaries, similar to the situation depicted in Fig. 3. The initial condition is as follows,

$$t = 0, \quad \rho = 1 + P'_{\max} \mathrm{e}^{-(\ln 2)(x^2+y^2+z^2)/r_0^2}, \quad u = U_0, \quad v = 0, \quad w = 0, \quad p = \frac{1}{\gamma} + P'_{\max} \mathrm{e}^{-(\ln 2)(x^2+y^2+z^2)/r_0^2}$$

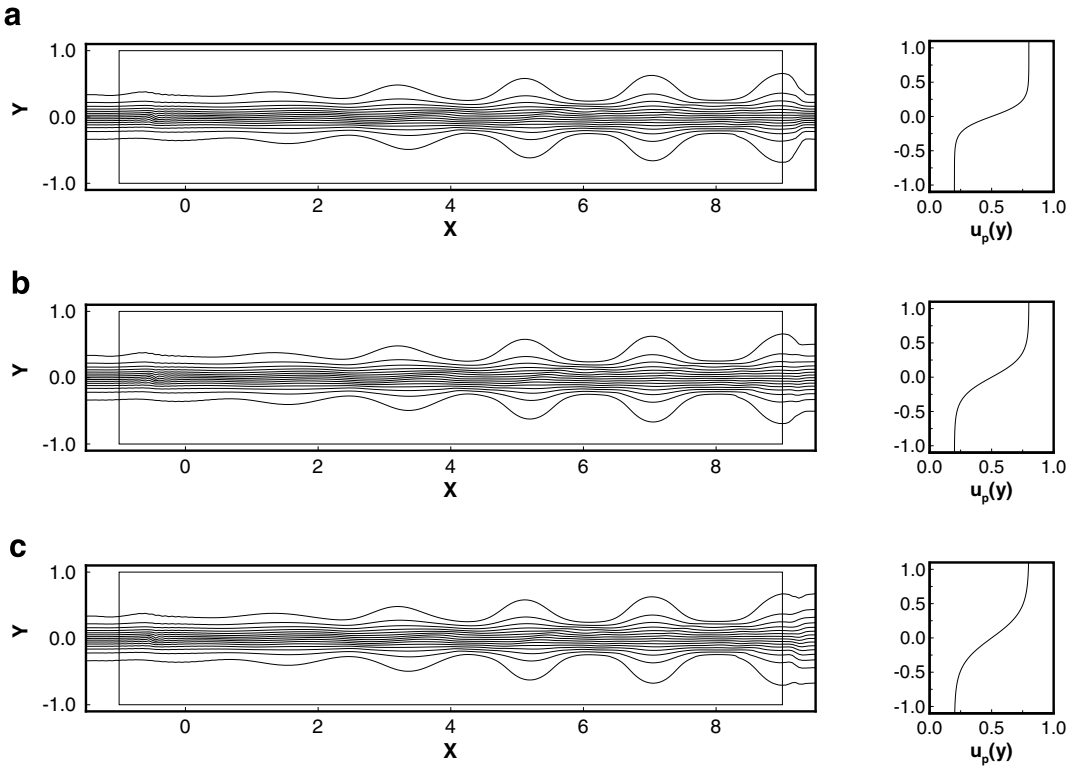

Fig. 21. Instantaneous u-velocity contours in three computations, using different pseudo mean flow thickness. (a) $\delta = 0.4$; (b) $\delta = 0.6$; (c) $\delta = 0.8$.

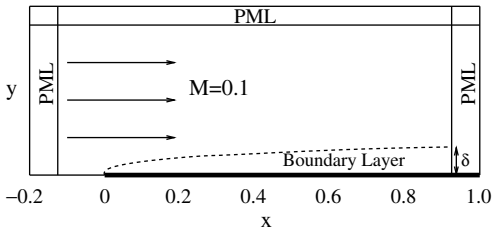

Fig. 22. Schematic of computational domain for the boundary layer computation.

where $\gamma = 1.4$, $r_0 = 1.0$, $U_0 = 0.5$, $P'_{\max} = 0.5$, and the Reynolds number is 500. The computational domain is $[-12, 12] \times [-12, 12] \times [-12, 12]$, including the PML domain, with a uniform mesh $\Delta x = \Delta y = \Delta z = 0.2$. The PML domains have a width of 10 grid points on all six sides and the maximum of PML absorption coefficients $\sigma_{\max}$ is 10. The pseudo mean flow is set as the uniform background flow with the value of $\beta = U_0/(1 - U_0^2)$.

Fig. 26 shows the pressure contours at $t = 8$ and 12. The effectiveness of the PML boundary condition is well demonstrated.

Fig. 27 shows the pressure at a point close to the outflow boundary, $(x, y, z) = (9, 0, 0)$, as a function of time. Very good agreement between the computational and reference solutions is observed. Also shown are the differences between the two solutions relative to the pulse strength $P'_{\max}$. For $P'_{\max} = 0.1, 0.2$ and 0.5, maximum relative reflection errors are all around 10^{-4}.

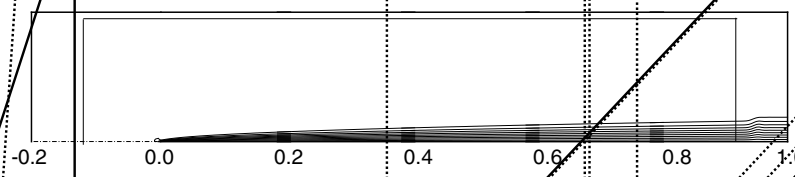

Fig. 24. Stream-wise velocity contours.

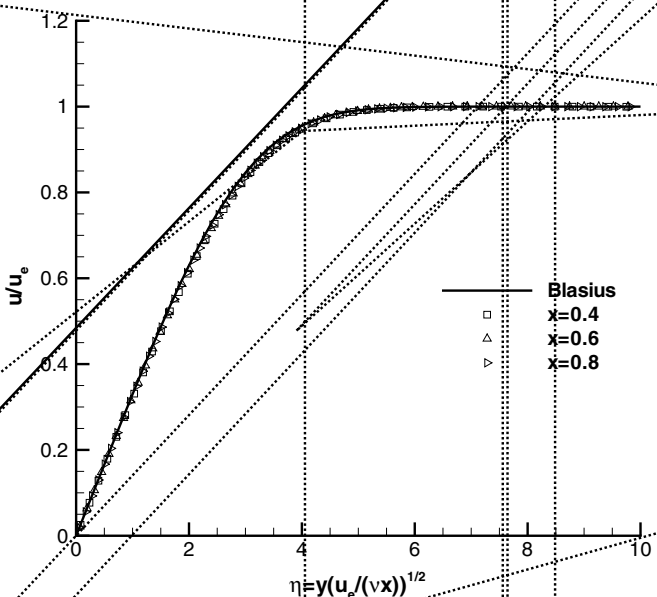

Fig. 25. Comparison with Blasius solution at $x = 0.4$, 0.6, 0.8. u_e is the exterior stream-wise velocity.

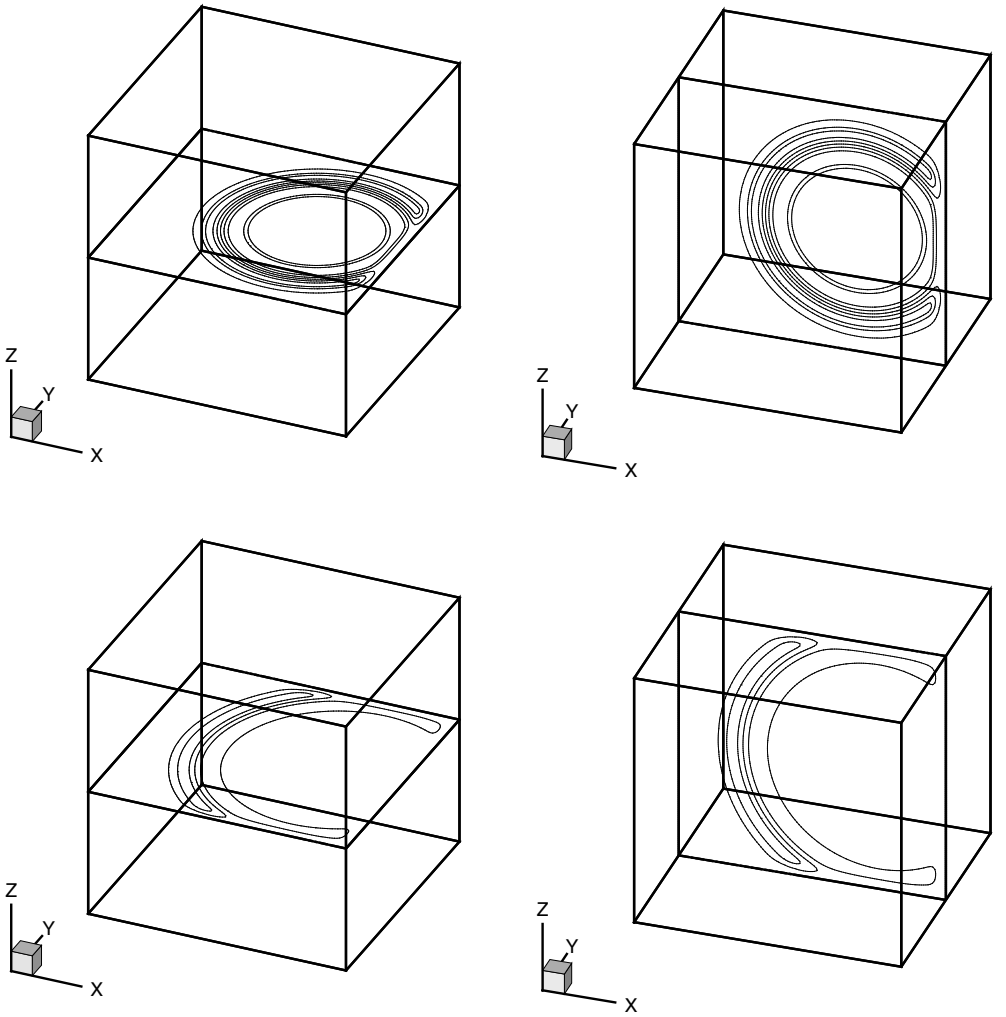

Fig. 26. Slices of pressure contours at $t = 8$ (top) and $t = 12$ (bottom).

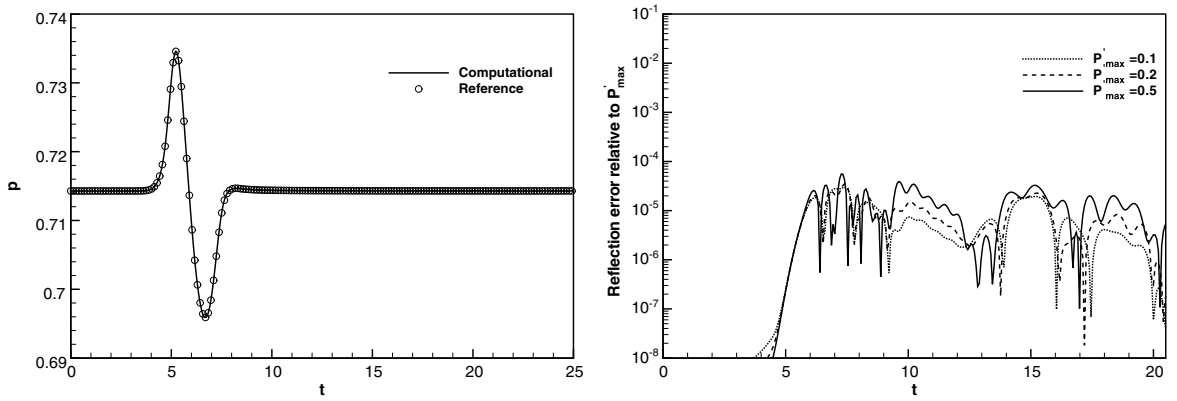

Fig. 27. Left: pressure at a point close to the boundary as a function of time; Right: relative reflection error in pressure compared with the large domain reference solution.

5. Conclusions

A time-domain absorbing boundary condition for the nonlinear Euler and Navier–Stokes equations has been presented following a recently developed method for the linearized Euler equations. It offers a natural extension of the linear PML equations to nonlinear equations of fluid dynamics. By introducing the concept of pseudo mean flow, the efficiency of PML is increased as it becomes only necessary to absorb the difference between the total variable and a prescribed pseudo mean flow. The pseudo mean flow is not required to be exactly the same as the actual mean flow when the latter is not available. Although the proposed equations are not theoretically perfectly matched to the nonlinear governing equations as their linear counter-parts are, numerical examples demonstrated their effectiveness as absorbing boundary conditions in truncating open boundaries in nonlinear Euler and Navier–Stokes simulations.

Since the proposed nonlinear equations reduce to the linear PML equations upon a linearization about the pseudo mean flow, the linear stability property of the PML proposed here is expected to be the same as those given in [19]. Although no numerical instability has been found in all our computations, theoretical property on the nonlinear stability remains to be defined. The success of PML for the fully nonlinear Euler and Navier–Stokes equations reported in the present paper is a significant step toward a wider application of the PML technique for computational fluid dynamics and computational aeroacoustics.

Acknowledgments

This work is supported by grants from the National Science Foundation DMS-0411402 (F.Q. Hu), the National Natural Science Foundation of China 50676003 and the 973 Program-2007CB714604 (X.D. Li and D.K. Lin), and the 111 Project B07009 of China. The authors also would like to thank the reviewers for constructive comments.

References

[1] S. Abarbanel, D. Gottlieb, J.S. Hesthaven, Well-posed perfectly matched layers for advective acoustics, Journal of Computational Physics 154 (1999) 266–283.
[2] D. Appelö, T. Hagstrom, G. Kreiss, Perfectly matched layers for hyperbolic systems: general formulation, well-posedness, and stability, SIAM Journal on Applied Mathematics 67 (1) (2006) 1–23.
[3] E. Becache, A.-S. Bonnet-Ben Dhia, G. Legendre, Perfectly matched layers for the convected Helmholtz equation, SIAM Journal on Numerical Analysis 42 (1) (2004) 409–433.
[4] E. Becache, S. Fauqueux, P. Joly, Stability of perfectly matched layers, group velocities and anisotropic waves, Journal of Computational Physics 188 (2003) 399–433.
[5] J.P. Berenger, A perfectly matched layer for the absorption of electromagnetic waves, Journal of Computational Physics 114 (1994) 185–200.
[6] W.C. Chew, W.H. Weedon, A 3D perfectly matched medium from modified Maxwell's equations with stretched coordinates, IEEE Transactions on Microwave and Optics Technology Letters 7 (1994) 599–604.
[7] F. Collino, P. Monk, The perfectly matched layer in curvilinear coordinates, SIAM Journal of Science, Computers 19 (6) (1998) 2016.
[8] S.D. Gedney, An anisotropic perfectly matched layer-absorbing medium for the truncation of FDTD lattices, IEEE Transactions on Antennas Propagation 44 (1996) 1630.
[9] T. Hagstrom, I. Nazarov, Absorbing layers and radiation boundary conditions for jet flow simulations, AIAA paper 2002-2606, 2002.
[10] T. Hagstrom, I. Nazarov, Perfectly matched layers and radiation boundary conditions for shear flow calculations, AIAA paper 2003-3298, 2003.
[11] T. Hagstrom, A new construction of perfectly matched layers for hyperbolic systems with application to linearized Euler equations, in: G.C. Cohen, E. Heikkola, P. Joly, P. Neittaanmaki (Eds.), Mathematical and Numerical Aspects of Wave Propagation — WAVES 2003, Springer, 2003, pp. 125–129.
[12] T. Hagstrom, J. Goodrich, I. Nazarov, C. Dodson, High-order methods and boundary conditions for simulating subsonic flows, AIAA paper 2005-2869, 2005.
[13] T. Hagstrom, D. Appelö, Experiments with Hermite methods for simulating compressible flows: Runge–Kutta time-stepping and absorbing layers, AIAA paper 2007-3505, 2007.
[14] M.E. Hayder, H.L. Atkins, Experiences with PML boundary conditions in fluid-flow computations, in: T.L. Geers (Ed.), IUTAM Symposium of Computational Methods for Unbounded Domains, Kluwer Academic Publishers, 1998, pp. 207–216.
[15] F.Q. Hu, M.Y. Hussaini, J.L. Manthey, Low-dissipation and -dispersion Runge–Kutta schemes for computational acoustics, Journal of Computational Physics 124 (1996) 177–191.

[16] F.Q. Hu, On absorbing boundary conditions of linearized Euler equations by a perfectly matched layer, Journal of Computational Physics 129 (1996) 201–219.
[17] F.Q. Hu, On perfectly matched layer as an absorbing boundary condition, AIAA paper 96-1664, 1996.
[18] F.Q. Hu, A. stable, Perfectly matched layer for linearized Euler equations in unsplit physical variables, Journal of Computational Physics 173 (2001) 455–480.
[19] F.Q. Hu, A perfectly matched layer absorbing boundary condition for linearized Euler equations with a non-uniform mean-flow, Journal of Computational Physics 208 (2005) 469–492.
[20] F.Q. Hu, On the construction of PML absorbing boundary condition for the nonlinear Euler equations, AIAA paper 2006-0798, 2006.
[21] F.Q. Hu, Development of PML absorbing boundary condition for computational aeroacoustics: a progress review, Computers & Fluids 37 (4) (2008) 336–348.
[22] X.D. Li, J.H. Gao, Numerical simulation of the three dimensional screech phenomenon from a circular jet, Physics of Fluids 20 (2) (2008), in press.
[23] X.D. Li, J.H. Gao, Numerical simulation of the generation mechanism of axisymmetric supersonic jet screech tones, Physics of Fluids 17, 2005 (Art No: 085105).
[24] F. Nataf, A new approach to perfectly matched layers for the linearized Euler system, Journal of Computational Physics 214 (2) (2006) 757–772.
[25] H. Schlichting, Boundary-layer Theory, McGraw-Hill, 1979.
[26] C.K.W. Tam, J.C. Webb, Dispersion-relation-preserving schemes for computational acoustics, Journal of Computational Physics 107 (1993) 262–281.
[27] E. Turkel, A. Yefet, Absorbing PML boundary layers for wave-like equations, Applied Numerical Mathematics 27 (1998) 533–557.
[28] L. Zhao, A.C. Cangellaris, GT-PML: generalized theory of perfectly match layers and its application to the reflectionless truncation of finite-difference time-domain grids, IEEE Transactions on Microwave Theory and Techniques 44 (1996) 2555–2563.